Xuewei Yan, Run' nan Wang, Qingyan Xu * and Baicheng Liu

Numerical Simulation and Experimental Casting of Nickel-Based Single-Crystal Superalloys by HRS and LMC Directional Solidification Processes

DOI 10.1515/htmp-2016-0116
Received June 14, 2016; accepted December 30, 2016

Abstract: Mathematical models for dynamic heat radiation and convection boundary in directional solidification processes are established to simulate the temperature fields. Cellular automaton (CA) method and Kurz-Giovanola-Trivedi (KGT) growth model are used to describe nucleation and growth. Primary dendritic arm spacing (PDAS) and secondary dendritic arm spacing (SDAS) are calculated by the Ma-Sham (MS) and Furer-Wunderlin (FW) models respectively. The mushy zone shape is investigated based on the temperature fields, for both high-rate solidification (HRS) and liquid metal cooling (LMC) processes. The evolution of the microstructure and crystallographic orientation are analyzed by simulation and electron back-scattered diffraction (EBSD) technique, respectively. Comparison of the simulation results from PDAS and SDAS with experimental results reveals a good agreement with each other. The results show that LMC process can provide both dendritic refinement and superior performance for castings due to the increased cooling rate and thermal gradient.

Keywords: nickel-based superalloy, directional solidification, liquid metal cooling, numerical simulation, microstructure

Introduction

Nickel-based superalloys are widely used in the aeronautic and energy industries because of their excellent mechanical properties at high temperature and corrosion resistance [1], and Nickel-based single-crystal superalloys exhibit even better comprehensive performances due to the elimination of grain boundary and strict control over the crystallographic orientation [2–4]. These characteristics make Nickel-based single-crystal superalloys the best choice for applications like aero-engine blades and industrial gas turbine (IGT) blades [5, 6], which are the limiting components to turbine inlet temperature and cycle efficiency [7]. Since Nickel-based single-crystal superalloy properties are largely dependent on the grain structure [8], a superior performance of the castings can be obtained by different solidification processes [9]. Generally, Nickel-based single-crystal superalloy components are produced by directional solidification processes [10], and the grain boundaries can be entirely removed by spiral grain selector geometry [11]. Nowadays, the major directional solidification process is the high-rate solidification (HRS) process [12], which provides a vertical temperature gradient by a water cooling chill-plate and a withdrawal unit [13]. This process has been highly optimized for the production of aero-engine scale components, which represent the majority of the production [14]. However, there are several issues when the HRS process is scaled to produce larger components [15], such as deformation and crack of mold shell, reaction of mold shell and liquid metal, and freckles, stray grain of castings. In recent years, several techniques have been proposed in order to solve these issues, such as liquid metal cooling (LMC) process [16, 17] and gas cooling casting (GCC) process [18]. Among them, LMC process is one of the best method, which improves heat extraction by immersing both casting and mold into a container of metal coolant with low melting temperature, as they are withdrawn from the heating zone [19]. As a powerful tool, numerical simulation technology can be used to study directional solidification processes, to predict final microstructures and optimize process parameters [20].

A lot of efforts have gone into the study of directional solidification technology by numerical simulation in the

***Corresponding author: Xu Qingyan,** Key Laboratory for Advanced Materials Processing Technology, Ministry of Education, School of Materials Science and Engineering, Tsinghua University, 100084 Beijing, China, E-mail: scjxqy@tsinghua.edu.cn
Xuewei Yan, Run' nan Wang, Baicheng Liu, Key Laboratory for Advanced Materials Processing Technology, Ministry of Education, School of Materials Science and Engineering, Tsinghua University, 100084 Beijing, China

last two decades [21–23]. Some of these studies were based on a commercial finite elements (FE) software ProCAST to simulate the solidification behavior, including mainly temperature distribution and thermal gradients [24–26]. In the 1990's, the cellular automaton (CA) method was introduced by Rappaz and Gandin [27–29] to simulate the microstructure of castings. Then, cellular automaton coupled finite elements (CAFE) became a comment method for simulating the temperature field and the microstructure of directional solidification castings. Recently, Wang et al. [11] simulated and analyzed the grain selection during single-crystal casting of a Nickel-based superalloy using the ProCAST & CAFE models with the HRS process. The results showed that there was no obvious correlation between crystallographic orientation and the parameters of the spiral passage. Miller et al. [17, 20, and 30] investigated the LMC process of castings through microstructure simulation, and proposed a lateral growth model for the microstructure. The model indicated that the enhanced heat extraction inherent to the process resulted in a curved solidification front that may lead to a non-axial dendrite growth near the casting walls.

In this study, an integrated macro and micro multiscale mathematical model based on dynamic heat radiation and modified cellular automaton finite difference (CAFD) method was developed to simulate the three-dimensional temperature fields and the microstructure evolution. The accuracy of this model was already validated in our previous study [31]. The pouring experiments were carried out using both HRS and LMC processes, in order to study their advantages and disadvantages. In addition, the grain crystallographic orientation and dendrite morphology were also investigated and analyzed. Based on simulation and experimental results, some guidelines for these two directional solidification processes have been determined.

Physical and mathematical models

Physical model

Schematic for HRS and LMC directional solidification furnaces are shown in Figure 1. The heating zone is generally divided into two parts, which provide a non-uniform temperature distribution along the vertical direction, whereas the cooling zone contains a water-cooling ring under the baffle of the HRS furnace; this ring is replaced by a low-melting-point, liquid metal coolant in the LMC furnace. The baffle can effectively prevent heat transfer between heating and cooling zones, and the float baffler is comprised of ceramic beads that float on the liquid metal coolant in the LMC furnace. The chill-plates consist of water-cooling copper and graphite for the HRS and LMC furnaces, respectively. A group of mold shells is fixed on the chill-plate, and the alloy is poured into the mold and maintained there for several minutes. Then, the withdrawal unit operates at an appropriate rate until the alloy completely solidifies.

Mathematical models

Macro heat transfer

The energy conservation equation was described as follows:

$$\rho c_{\mathrm{p}} \frac{\partial T}{\partial t} = \lambda \cdot \nabla^2 T + \rho \Delta H \frac{\partial f_{\mathrm{s}}}{\partial t} + Q_{\mathrm{R}} \tag{1}$$

where T is the temperature, t is the time, ρ is the density, c_{p} is the specific heat, ΔH is the latent heat, λ is the heat conductivity, f_{s} is the mass fraction of the solid phase, and Q_{R} is the heat exchange between the casting surface and the environment.

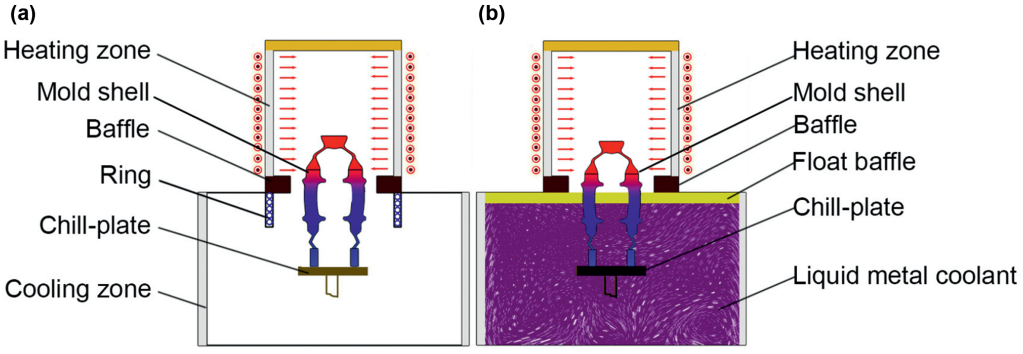

Figure 1: Simplified schematic diagrams for the directional solidification furnaces: (a) HRS and (b) LMC.

The heat transfer is complex during directional solidification processes; hence, an integrated boundary condition was defined to simulate the macro temperature distribution. A modified Monte Carlo-based [32] ray tracing model was adopted to deal with the heat radiation between every two discrete surfaces, with the Q_R being calculated as follows:

$$Q_R = \sigma \sum_{n=1}^{N} \frac{\beta_n \left(T^4 - T_n^4\right)}{\frac{1-\varepsilon}{\varepsilon} + \frac{(1-\varepsilon_n)S}{\varepsilon_n S_n} + 1} \tag{2}$$

where σ is the Stefan-Boltzmann constant, N is the ray line number, equaling 50, β_n is the energy factor of n, T and T_n are the temperature of different solid elements, ε is the blackness coefficient, S_n is the standard surface areas of element, equaling 1 mm^2, and S is practical surface areas of element, about 0.49 mm^2.

The heat transfer pattern varied from radiation to conduction as the shell mold was descended into the cooling zone during the LMC process. Therefore, the Q_R can be described by the following equations at this stage.

$$Q_R = h_a(T - T_a) \tag{3}$$

$$Q_R = h_b(T - T_b) \tag{4}$$

where h_a and h_b are the heat transfer coefficients of the shell mold with the float baffle, and liquid metal coolant, respectively; T_a and T_b are the temperatures of the float baffle, and the liquid metal coolant, respectively.

Microstructure nucleation and growth

The microstructure simulation was based on the modified CA method [33]. A stochastic nucleation model was established to calculate the number of nucleus as follows:

$$\frac{\partial N}{\partial(\Delta T)} = \frac{N_s}{\sqrt{2\pi}\Delta T_\sigma} \exp\left[-\frac{(\Delta T - \Delta T_N)^2}{2(\Delta T_\sigma)^2}\right] \tag{5}$$

where N is the nucleus density, ΔT is the undercooling, N_s is the maximum nucleus density, ΔT_σ is the standard deviation of the distribution, and ΔT_N is the average nucleation undercooling. Then, the grain density can be described as follows:

$$N(\Delta T) = \int_0^{\Delta T} \frac{dN}{d(\Delta T')} d(\Delta T') \tag{6}$$

where the ΔT ' is the integral unit of undercooling.

The grain growth was based on the Kurz-Giovanola-Trivedi (KGT) equation [34], and the growth speed of the grain tip is described as follows:

$$v(\Delta T) = \alpha \cdot \Delta T^2 + \beta \cdot \Delta T^3 \tag{7}$$

where α and β are the coefficients.

Dendritic arm spacing

Dendritic arm spacing has an important influence on the castings performance. However, the dendritic arm spacing, which varies during directional solidification, and has not been satisfactorily described thus far. In this study, Ma-Sham (MS) [35] and Furer-Wunderlin (FW) models [36] were used to simulate the primary dendritic arm spacing (PDAS, λ_1) and secondary dendritic arm spacing (SDAS, λ_2) respectively, and the equations are simplified as follows:

$$\lambda_1 = 2\pi(kD\Gamma\Delta T_0)^{1/4}\left(1 - \frac{V_c}{V}\right)^{3/4} G^{-(1/2)} V^{-(1/4)} \tag{8}$$

$$\lambda_2 = \left(166 \frac{\Gamma D ln(c_{eut}/c_0)}{m(1-k)(c_0 - c_{eut})} \cdot t_f\right)^{1/3} \tag{9}$$

where k is the solute partition coefficient equaling 0.788, D is the diffusion coefficient, equaling 3.6×10^{-9} m$^2 \cdot$ s^{-1} , Γ is the Gibbs-Thompson factor, 3.65×10^{-7} $k \cdot$ m, V_c is the critical velocity 10 °C·s^{-1} for HRS and 30 °C $\cdot$ s^{-1} for LMC, V is the cooling velocity, G is the temperature gradient, 10 °C $\cdot$ mm^{-1} for HRS and 30 °C $\cdot$ mm^{-1} for LMC, m is the liquidus slope equaling −3.95, c_{eut} is the eutectic composition, c_0 is the initial concentration, and t_f is the local solidification time.

Experimental and simulation details

The pouring experiment is carried out with a 10 kg HRS&LMC amphibious directional solidification furnace, and the liquid metal coolant in the LMC process is tin. The casting configuration is a modified six-bar cluster mold (Figure 2(a)); the nominal diameter and height for each bar are 15 mm and 220 mm, respectively. DD6 (Ni-4.3Cr-9Co-2Mo-8W-7.5Ta-2Re-0.5Nb- 5.6Al-0.1Hf, wt. %) superalloy is hold at 1,823 K in a crucible, and the ceramic shell mold is preheated at 1,793 K. The castings then grow with withdrawal rate of 4 and 8 mm·min^{-1} for the HRS and LMC processes, respectively. After solidification and removal from the mold, one of the bars is sectioned along transverse and parallel to the growth direction in order to evaluate the dendrite spacing and morphology at specific locations within the castings (Figure 2(b)). Following metallographic preparation, polished surfaces are etched to reveal the dendritic structure using a solution containing 70 mL CH_3CH_2OH, 30 mL HCl and 2.5 g $CuCl_2$. Electron back-scattered diffraction (EBSD) technique is carried to analyze the crystallographic orientation of the grains. Dendrite morphology of the castings with different processes is observed using a LEICA DM6000M optical microscope.

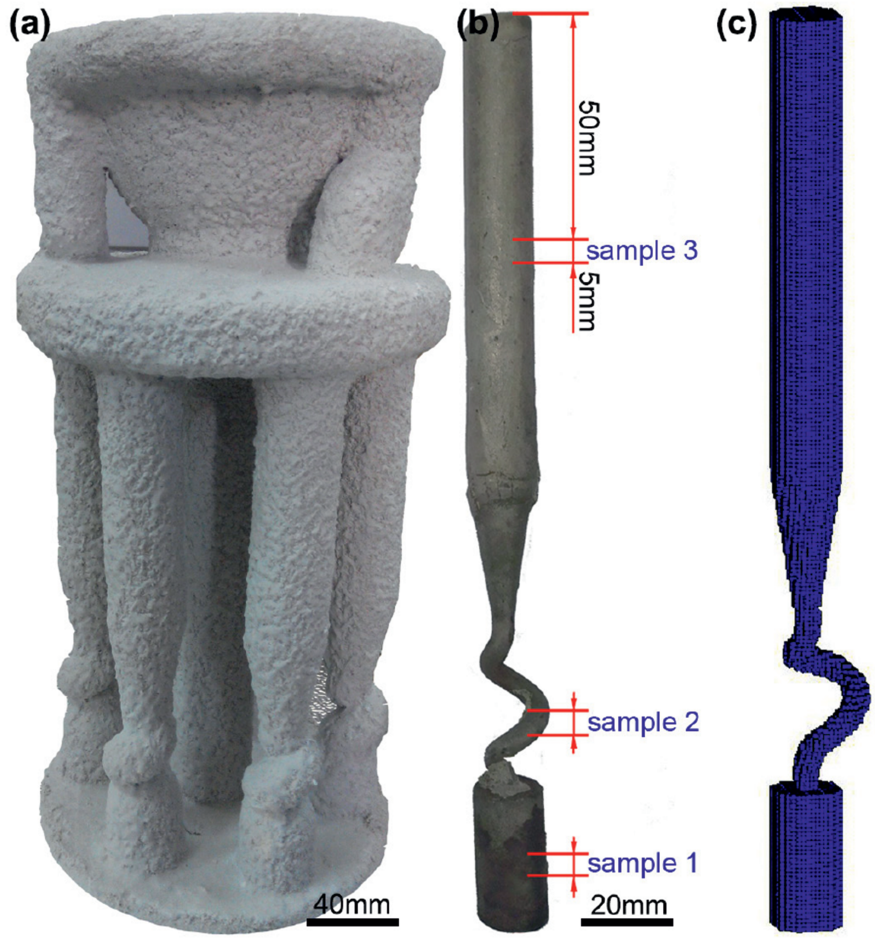

Figure 2: (a) Mold configuration; (b) Location of the sectioned specimens in the single bar; (c) Mesh of the single bar.

In order to provide insight into the temperature distribution and microstructure evolution, the directional solidification process was simulated using the CAFD model, and the three-dimensional mesh of the cast is shown in Figure 2(c). Some key parameters and their corresponding values are summarized in Table 1. For each simulation, the temperature field, grain structure, and dendritic arm spacing were calculated to compare with the experimental results.

Table 1: Key parameters and values for simulation [5, 20].

Thermo-physical property	Value
Liquidus temperature	1,672 K
Solidus temperature	1,615 K
Thermal conductivity	0.0332 kJ · m^{-1} · s^{-1} · K^{-1}
Density	8,780 kg · m^{-3}
Specific heat	0.773 kJ · kg^{-1} · K^{-1}
Interface heat transfer coefficient	*Value*
Cast-shell	750 W · $m^{-2}K^{-1}$
Cast-chill	3,000 W · $m^{-2}K^{-1}$
Shell-Tin	4,000 W · $m^{-2}K^{-1}$
Boundary conditions	*Value*
Shell emissivity	0.4
Baffle emissivity	0.2
Tin temperature	523 K

Results and discussion

Simulation of the mushy zone

Based on the results of the temperature distribution, the mushy zone evolution can be obtained. The mushy zone is defined as the zone where the temperature is between the liquidus and solidus, which ranges from 1,615 to 1,672 K for the DD6 superalloy. In order to investigate the characteristics of the mushy zone, several solid

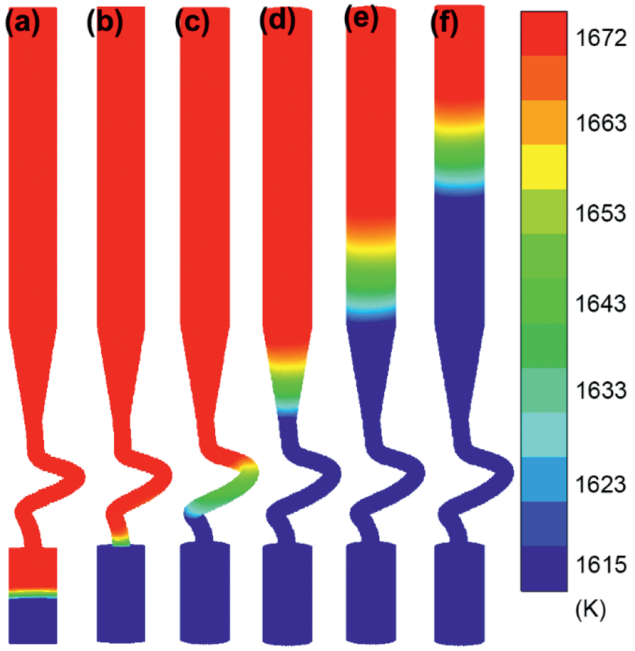

Figure 3: Mushy zone distribution of Ni-based casting samples for the HRS process: (a) $t = 30$ s, $f_s = 10$ %; (b) $t = 78$ s, $f_s = 20$ %; (c) $t = 157$ s, $f_s = 22$ %; (d) $t = 1{,}337$ s, $f_s = 27$ %; (e) $t = 1{,}755$ s, $f_s = 45$ %; (f) $t = 2{,}125$ s, $f_s = 70$ %.

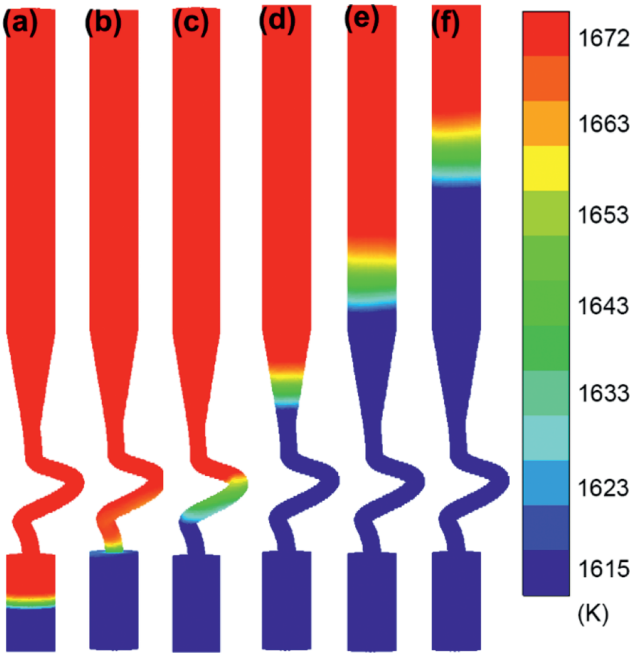

Figure 4: Mushy zone distribution of Ni-based samples for the LMC process: (a) $t = 90$ s, $f_s = 10$ %; (b) $t = 132$ s, $f_s = 20$ %; (c) $t = 145$ s, $f_s = 22$ %; (d) $t = 672$ s, $f_s = 27$ %; (e) $t = 965$ s, $f_s = 45$ %; (f) $t = 1{,}254$ s, $f_s = 70$ %.

fractions (10, 20, 22, 27, 45, and 70 %) were chosen to show the variation tendency for the HRS (Figure 3) and LMC process (Figure 4). At an initial stage, the heat is dissipated through the chill-plate, so the thermal gradient near the chill was high and the mushy zone was narrow and horizontal. As the withdrawal process continued, the heat dissipation changed to heat conduction for the LMC process and heat radiation for HRS process, so the mushy zone became wider and more flexible. Afterwards, the mushy zone for the LMC process became narrower and more horizontal compared with that of the HRS process, because the efficiency of heat radiation for the HRS was much lower than that of heat conduction in the LMC process. Therefore, there was not enough time to dissipate the heat, as the heat transfer and length of the mushy zone appeared enlarged near the end of the solidification.

In order to study the mushy zone in detail, the concavity (K_{con}) and the length (K_d) of mushy zone were calculated using the following equations [37]:

$$K_{con} = \iint_S \frac{(OP \times Z_0) \cdot (G_p \times Z_0)}{|OP||G_P|} dxdy \tag{10}$$

$$K_d = V_m / S \tag{11}$$

where G_p is the temperature gradient, O is the geometric center point, Z_0 is the vertical up unit vector, P is the point with neighborhood $dxdy$, V_m is the volume between two different isothermal surfaces, and S is the projection area of V_m.

Figure 5(a) shows the mushy zone concavity increasing continuously with the distance to chill, with the exception of some small fluctuations caused by a non-uniform heat transfer. The mushy zone concavity in the LMC process remained relatively stable compared with that in the HRS process. Figure 5(b) shows the mushy zone length variation with the distance to chill. Initially, the length of the mushy zone for the LMC process were slightly wider than that for the HRS process, because the cooling effect of the water-cooling plate in HRS was more significant than that of the graphite plate in LMC. However, the variation tendency of the mushy zone length was inverted as the heat transfer mode changed into conduction and radiation for the LMC and HRS processes, respectively. Studies [20, 30] showed that narrow and horizontal mushy zones were important to improve the quality of microstructure. Therefore, castings produced by the LMC process were superior to those obtained by the HRS process.

Grain selection behavior

The grain selector is the key component in single-crystal casting and includes two parts, *i. e.* a starter block and

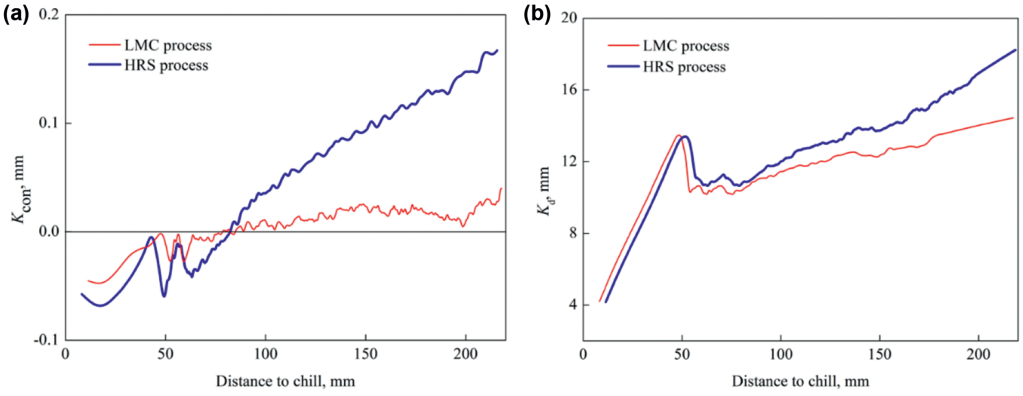

Figure 5: Mushy zone variation with distance to chill: (a) concavity and (b) length.

the spiral part, known as "pigtail". The former provides the space for nucleation and grain competitive growth, whereas the latter provides a special tunnel that blocks most grains, allowing only one to grow. In this study, grain selection behavior was studied by comparing experimental and simulation data. The grain competitive growth and elimination was very complex, and given the difficulty in monitoring the experimental data, the simulation played an important role in predicting the effectiveness of the spiral selector. The grain evolution at different solidification times and the experimental results are shown in Figures 6 and 7 (HRS and LMC process, respectively). Different colors were used to mark the different grains in the simulation results.

The results showed that the nucleation took place at the bottom of the starter block, and then these small nuclei grew in the opposite direction of the heat flow. Only a few grains remained in the starter block and grew to a certain size. As these grains continually grew and became coarse, other grains, which were not well aligned along with the maximum thermal gradient, grew at a much slower rate due to the restriction by the well-aligned grains, and were finally eliminated. At the top of the starter block, just one grain remained in the pigtail, which grew bigger and finally occupied the whole casting at the top of the spiral part.

The columnar grains were coarse and sparse in the LMC process compared with those in the HRS during the

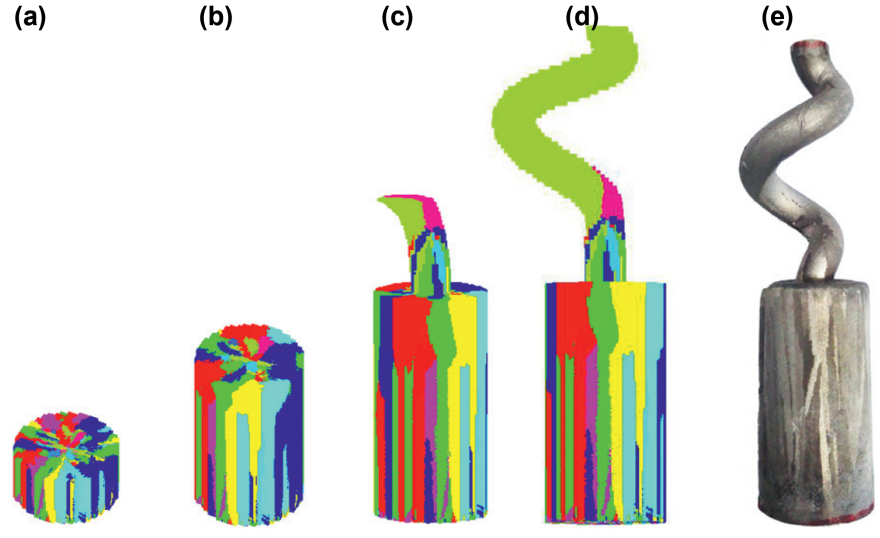

Figure 6: Simulation and experimental results of the grain structure for the HRS process: (a) $t = 30$ s; (b) $t = 60$ s; (c) $t = 90$ s; (d) $t = 180$ s; and (e) experimental result.

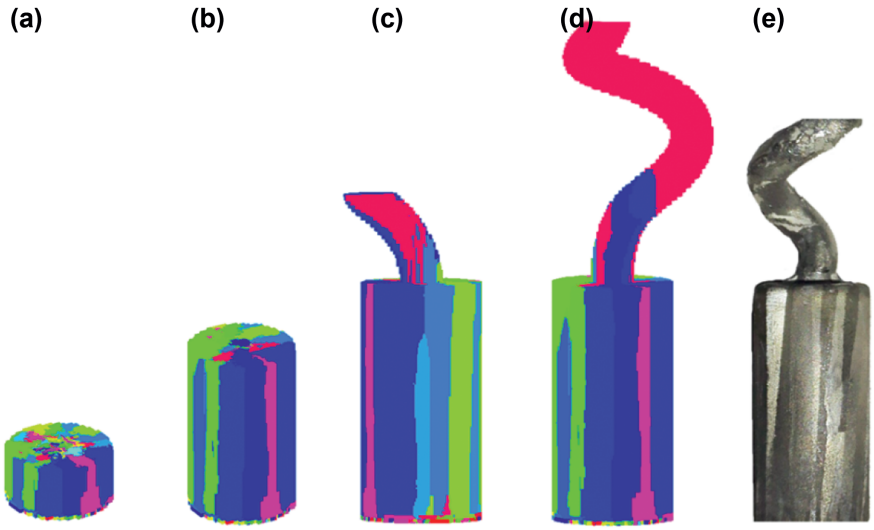

Figure 7: Simulation and experimental results of the grain structure for the LMC process: (a) $t = 90$ s; (b) $t = 120$ s; (c) $t = 150$; (d) $t = 180$ s; and (e) experimental result.

starter block, as the chilling action of graphite in LMC was weaker than water-cooling copper in HRS. Hence, grains will be more likely to grow if the cooling rate is decreased. However, single-crystal selection becomes more difficult due to the number of grains competing for growth. Therefore, the LMC process was superior to the HRS one regarding grain selection. Hence, the results of these two different processes indicated that the geometry of the grain selector was crucial to produce a single-crystal casting for the Ni-based DD6 superalloy, and the simulation and experimental results were in good agreement with each other.

The preferred growth direction of the nickel-based superalloys was <001>, as a deviation of the preferred growth direction from the heat direction greatly influences the mechanical properties. EBSD technique was used to observe the crystallographic orientation of the samples (Figure 8). It showed that the crystallographic orientation had a significant variation during the entire directional solidification process. Many grains grew competitively and disorderly in the beginning of the process, whereas other grains shrank or disappeared rapidly in the spiral section, where only one grain was preserved in the end. Therefore, the crystallographic orientation of the single-crystal section was well ordered. The average deviation angle of the cast samples was investigated by comparing simulation and experimental data in both processes (Figure 9). According to Figure 9, the measured deviation angles were in good agreement with the simulation results. In addition, the average deviation angle in the samples produced by the HRS process was bigger than that obtained by the LMC process. It is suggested that by employing the LMC process, it was possible to produce nickel-based single-crystal superalloy components possessing an improved crystallographic orientation.

Dendritic arm spacing

Dendritic arm spacing is the typical measurement to help quantify the fineness of the microstructure, and it is a powerful tool to control the morphology and microstructural characteristics, and improve the properties of castings in directional solidification. Based on the theoretical models of MS and FW, PDAS and SDAS were calculated (Figure 10). It can be observed that the PDAS and SDAS were small at the beginning of the directional solidification process, and became coarse with the dendrites growth. In the spiral section, some of the dendrites developed secondary branching, while others were suppressed, so the SDAS in the spiral section was very small. At the top of the single-crystal bar, PDAS and SDAS became wider as the growth velocity of dendrites tip was slower. In addition, PDAS and SDAS in the LMC process were fine and became less visible compared to those in the HRS process. This is because the microstructure formation during directional solidification was dependent on the local thermal field, specifically the thermal gradient and solidification rate.

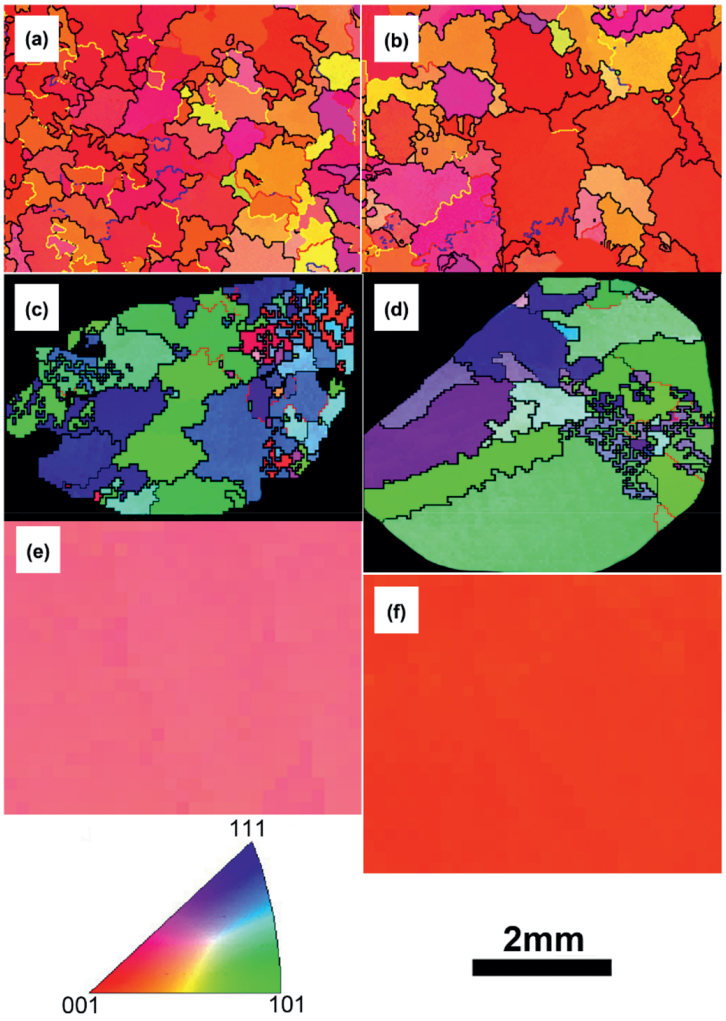

Figure 8: EBSD results on the grain structure of different samples: (a), (c) and (e) the HRS process; (b), (d) and (f) the LMC process.

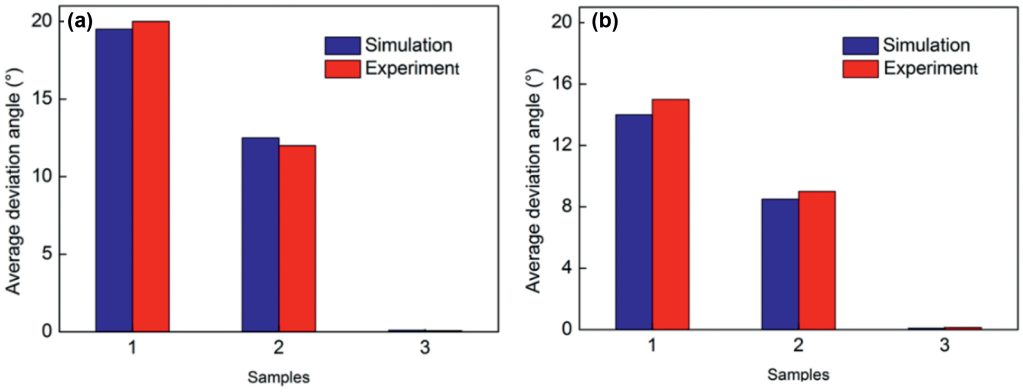

Figure 9: Simulation and experimental results of the average deviations angles: (a) HRS and (b) LMC process.

Therefore, during the directional solidification process, variations to the local thermal conditions can affect the stability of the progressing solidification front and cause variations in dendrite morphology and the formation of defects. The LMC process can offer a refinement of the dendritic structure due to the increased cooling rate and thermal gradient compared with the HRS process.

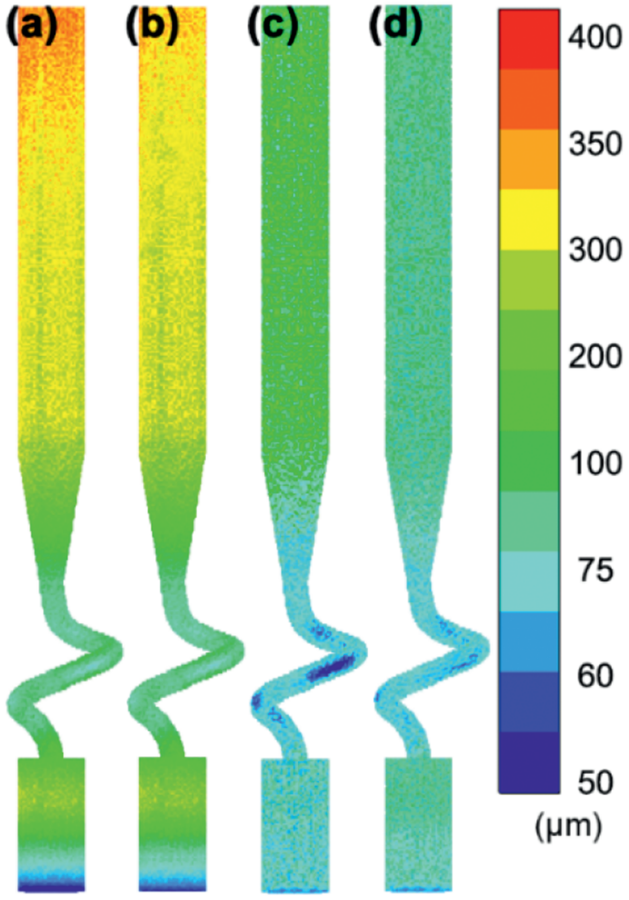

Figure 10: Morphology of the dendritic arm spacing: (a) PDAS in the HRS process; (b) PDAS in the LMC process; (c) SDAS in the HRS process; and (d) SDAS in the LMC process.

The rod samples produced by the HRS and LMC processes were both sectioned according to Figure 1(b), and the as-cast dendritic morphology was analyzed at three locations: in the starter block, in the spiral section, and in the single-crystal section as shown in Figure 11(a), (c), and (e) for the HRS process, and (b), (d), and (f) for the LMC process. A similar dendritic morphology was observed in sample (a) and sample (b), where the dendrites were fine and non-orientated, and there were many crystal boundaries in different areas. In the spiral section (samples (c) and (d)), the dendrites became coarse and the crystal boundaries reduced. At the location of the samples (e) and (f), the dendrite structures remained a single-crystal. However, a difference was observed between samples from the HRS and LMC processes. The size of the dendrites increased significantly more in different stages during the HRS process, while it was less pronounced for the LMC one. As identified previously, the thermal conditions were different between the HRS and LMC processes. There was a higher thermal gradient at the beginning of the HRS directional solidification process, due to the action of the water-cooling plate, decreasing with the increase in height. However, the thermal gradient was barely reduced as the action of the liquid metal coolant. Thus, the LMC process is superior to the HRS one regarding the dendritic structure refining.

Figure 12 shows the comparison between simulation and experimental results for PDAS and SDAS from both HRS and LMC processes. While the agreement was remarkable, the distance for the simulation range was ~1 mm, which was a relatively small distance, and it was expected that under these conditions the errors were not significant. It was noticed that PDAS increased with the distance to chill early in the directional solidification, then reduced to a constant value about 200 μm in the spiral section. In the single-crystal section, PDAS was ~330 μm for the HRS process and 300 μm for the LMC. SDAS reached a minimum in the spiral section, and coarsening was not significant in the rest of the process, the values were ~75 μm for the HRS process and 70 μm for the LMC.

Conclusions

The LMC directional solidification process was compared to the conventional HRS process both from a theoretical and experimental point of view. The temperature field distribution, crystallographic orientation, and dendritic arm spacing were analyzed for the HRS and LMC processes. The combined simulation and experimental investigation demonstrated the following:

(1) Mathematical models for dynamic heat radiation and convection boundary in directional solidification process were established to simulate the three-dimensional temperature field; CA method and KGT growth model were used to describe the nucleation and growth of the grain structure. PDAS and SDAS were calculated by using the MS and FW models for both HRS and LMC processes.

(2) Based on temperature field, the evolution of the mushy zone was investigated, including the concavity and the length. The mushy zone shape was narrower and more horizontal in the LMC process than in the HRS one.

(3) Grain growth and crystallographic orientation were studied by comparing simulation and experimental data, and the results are in good agreement with each other. LMC process provided a large thermal

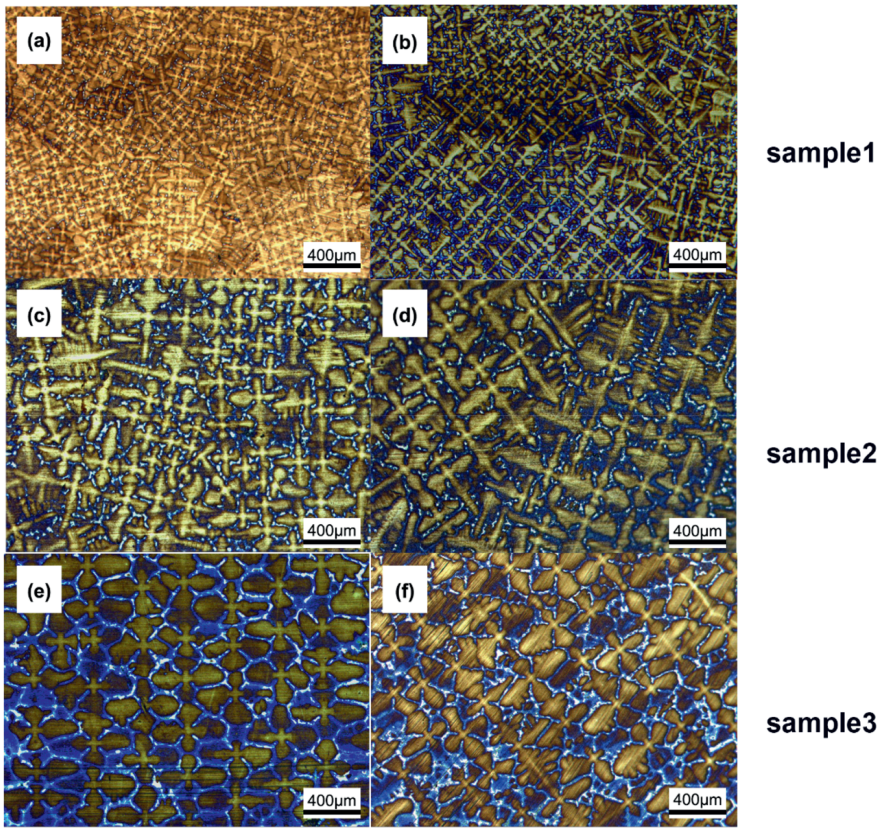

Figure 11: Transverse micrographs of samples in different locations: (a), (c) and (e) for the HRS process; (b), (d) and (f) for the LMC process.

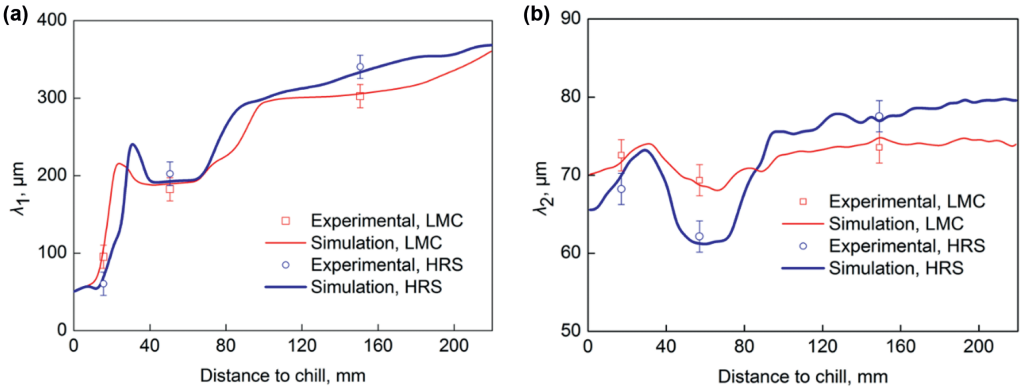

Figure 12: Comparison between simulation and experimental results: (a) PDAS and (b) SDAS.

gradient, and the average deviation angle of casting was smaller than that in the HRS process.

(4) The dendrite growth was investigated for both HRS and LMC processes, and the range of PDAS and SDAS was compared. More refined dendrites were observed in the samples produced by the LMC process.

Funding: This research was funded by the National Basic Research Program of China (nos. 2011CB706801), National Natural Science Foundation of China (nos. 51171089, 51374137), National Science & Technology Major Projects (nos. 2012ZX04012-011, 2011ZX04014-052, and 2009ZX04006-041).

References

[1] D. Pan, Q.Y. Xu, J. Yu, B.C. Liu, J.R. Li, H.L. Yuan and H.P. Jin, Int. J. Cast Metal. Res., 21 (2008) 308–312.
[2] M. Rappaz, Curr. Opin. Solid State Mater. Sci., 20 (2015) 37–45.
[3] X.B. Hu, Y.L. Zhu, N.C. Sheng and X.L. Ma, Sci. Rep., 4 2014) 7367–7375.
[4] M. Asta, C. Beckermann, A. Karma, W. Kurz, R. Napolitano, M. Plapp, G. Purdy, M. Rappaz and R. Trivedi, Acta Mater., 57 (2009) 941–971.
[5] H. Zhang, Q.Y. Xu and B.C. Liu, Mater, 7 (2014) 1625–1639.
[6] A.J. Elliott, S. Tin and W.T. King, Metall. Mater. Trans. A., 35A (2004) 3221–3231.
[7] A. Kermanpur, M. Mehrara, N. Varahram and P. Davami, Mater. Sci. Technol., 24 (2008) 100–106.
[8] Y.Z. Zhou, A. Volek and N.R. Green, Acta Mater., 56 (2008) 2631–2637.
[9] T.J. Fitzgerald and R.F. Singer, Metall. mater. trans. A, 28 (1997) 1377–1383.
[10] A.F. Giamei and J.G. Tschinkel, Metall. trans. A, 7 (1976) 1427–1434.
[11] N. Wang, L. Liu, S. Gao, X. Zhao, T. Huang, J. Zhang and H. Fu, J. Alloys Compd., 586 (2014) 220–229.
[12] P.W. Bridgman. US Pat, 88650, 1926.
[13] D. Pan, Q.Y. Xu and B.C. Liu, Sci. China Phys. Mech. Astron., 54 (2011) 851–855.
[14] H. Zhang, Q. Xu, N. Tang, D. Pan and B. Liu, Sci. China, 54 (2011) 3191–3202.
[15] A. Kermanpur, M. Rappaz, N. Varahram and P. Davami, Metall. Mater. Trans. B, 31B (2000) 1293–1304.
[16] K. Zhao, Y.H. Ma and L.H. Lou, J Alloys Compd., 475 (2009) 648–651.
[17] J.D. Miller, L. Yuan, P.D. Lee and T.M. Pollock, Acta Mater., 69 (2014) 47–59.
[18] D. Ma and A. Bührig-Polaczek, Metall. Mater. Trans. B, 40 (2009) 738–748.
[19] C.L. Brundidge, J.D. Miller and T.M. Pollock, Metall. Mater. Trans. A, 42 (2011) 2723–2732.
[20] J.D. Miller and T.M. Pollock, Acta Mater., 78 (2014) 23–36.
[21] L. Yuan, P.D. Lee, G. Djambazov and K. Pericleous, Int. J. Cast Metal. res., 22 (2009) 204–207.
[22] H.B. Dong and P.D. Lee, Acta Mater., 53 (2005) 659–668.
[23] S. Karagadde, L. Yuan, N. Shevchenko, S. Eckert and P.D. Lee, Acta Mater., 79 (2014) 168–180.
[24] I.M. McKenna, S.O. Poulsen, E.M. Lauridsen, W. Ludwig and P.W. Voorhees, Acta Mater., 78 (2014) 125–134.
[25] G. Lv, D. Chen, X. Yang, W. Ma, T. Luo, K. Wei and Y. Zhou, Vac, 116 (2015) 96–103.
[26] Z.H. Jia, L. Xu, R. Tao, M.Z. Ma, D.C. Xie and Y.T. Zhao, Appl. Mech.Mater., 723 (2015) 561–564.
[27] C.A. Gandin and M. Rappaz, Acta Mater., 45 (1996) 2187–2195.
[28] C.A. Gandin and M. Rappaz, Acta Metall. Mater., 42 (1994) 2233–2246.
[29] C.A. Gandin and M. Rappaz, Acta Metall. Mater., 41 (1993) 345–360.
[30] J.D. Miller and T.M. Pollock, Metall. Mater. Trans. A, 45 (2014) 411–425.
[31] X.W. Yan, N. Tang, X.F. Liu, G.Y. Shui, Q.Y. Xu and B.C. Liu, Acta Metall. Sin., 51 (2015) 1288–1296.
[32] Q.Y. Xu, B.C. Liu, D. Pan and J. Yu, China Foundry, 9 (2012) 69–77.
[33] C.A. Gandin, J.L. Desbiolles, M. Rappaz and P. Thévoz, Metall. Mater. Trans. A, 30A (1999) 3153–3165.
[34] W. Kurz, B. Giovanola and R. Trivedi, Acta Metall., 34 (1986) 823–830.
[35] D. Ma, Metall. Mater. Trans. B, 33 (2002) 223–233.
[36] N. Tang, X.W. Yan, Q.Y. Xu and B.C. Liu, Foundry, 63 (2014) 347–351.
[37] N. Tang, Y.L. Wang, Q.Y. Xu, X.H. Zhao and B.C. Liu, Acta Metall. Sin., 51 (2015) 499–512.